
Article:
Azam, M, Yue, S, Xu, R et al. (11 more authors) (2020) Realization of Moisture-Resistive Perovskite Films for Highly Efficient Solar Cells Using Molecule Incorporation. ACS Applied Materials & Interfaces, 12 (35). pp. 39063-39073. ISSN 1944-8244

https://doi.org/10.1021/acsami.0c09046

Realization of Moisture Resistive Perovskite Film for High Efficient Solar Cells using Molecule Incorporation

Muhammad Azam [a,b,c], Shizhong Yue [a,b], Rui Xu [d], Shuaijian Yang [a,b], Kong Liu [a,b], Yanbin Huang [a,b], Yang Sun [a,b], Ali Hassan [e], Kuankuan Ren [a,b], Furui Tan [f], Zhijie Wang [a,b,], Yong Lei [d,*], Shengchun Qu [a,b,*] and Zhanguo Wang [a,b]*

[a] Key Laboratory of Semiconductor Materials Science, Beijing Key Laboratory of Low Dimensional Semiconductor Materials and Devices, Institute of Semiconductors, Chinese Academy of Sciences, Beijing, 100083, China.

[b] Center of Materials Science and Optoelectronics Engineering, University of Chinese Academy of Sciences, Beijing 100049, China.

[c] Shenzhen Key Laboratory of Advanced Thin Films and Applications, College of Physics and Optoelectronic Engineering, Shenzhen University, Shenzhen, 518060, P. R China.

[d] Institut für Physik & IMN MacroNano@ (ZIK), Technische Universität Ilmenau, 98693 Ilmenau, Germany.

[e] Key Laboratory of Optoelectronic Devices and Systems of Guangdong Province & Ministry of Education, College of Physics and Optoelectronic Engineering Shenzhen University Shenzhen 518060, China.

[f] Key Laboratory of Photovoltaic Materials, Department of Physics and Electronics, Henan University, Henan, 475004 China.

ABSTRACT

The development of high-crystalline perovskite films with large crystal grains and few surface-defects is attractive to obtain high performance perovskite solar cells (PSCs) with good device stability. Herein, we simultaneously improve the power conversion efficiency (PCE) and humid stability of the $CH_3NH_3PbI_3$ (CH_3NH_3=MA) device by incorporating small organic molecule IT-4F to the perovskite film and using buffer layer of PFN-Br. The presence of IT-4F in the perovskite film can successfully improve crystallinity and enhance grain size, leading to reduced trap states, longer lifetime of charge carrier and make perovskite film hydrophobic. Meanwhile, as a buffer layer, PFN-Br can accelerate the separation of exciton and promote the collection process of electrons from active layer to cathode. As a consequence, the PSCs present a remarkably improved PCE to 20.55% with reduced device hysteresis. Moreover, the moisture resistive film based devices retain about 80% of its initial efficiency after 30 days of storage in relative humidity (RH) of 10-30% without encapsulation.

KEYWORDS : IT-4F, stability, defect states, hysteresis, crystallization

Introduction

Remarkable optical and electrical characteristics, such as tunable band gap, high absorption coefficient, ambipolar carrier transport character, weak excitation binding energy, above micron carrier diffusion length, and low-cost processability, make organometal halide perovskite materials a promising candidate for next-generation optoelectronic devices [1-6]. Tremendous researches have been done to improving the PCE of PSCs, resulting in the extraordinary enhancement in PCE certified 25.2% in just 10 years [7-8]. The rapid improvement in PCE makes this technology comparable to the commercialized photovoltaic technology, such as crystalline silicon solar cells, enabling it to be highly impressive in the future market of solar cells [9-10].

Homogeneous perovskite films with high-quality crystallization and suitable energy level alignment are critically important to assurance sufficient light harvesting, inhibit the recombination of photo-excited excitons and promote the collection process of electron/hole synchronously [11-12]. However, in polycrystalline perovskite films the recombination lifetime of charge carrier much shorter than that of its single crystal suggests that the film has a large number of grain boundaries due to which the polycrystalline film contains a large density of ionic or surface defects [13-16]. Along with the improvement in PCE of conventional $MAPbI_3$-based devices, the topics of long-term environment stability and hysteresis are of intense interest. Perovskite film quality is related to the device stability, including moisture stability, light stability and thermal stability [17-19]. Specifically, since the $MAPbI_3$ halide perovskites have a highly ionic character, MA^+ can quickly decompose under moisture conditions without full encapsulation [20]. The penetration of oxygen or moisture molecule into the perovskite film through the defects at the grain boundaries is responsible for device degradation [21]. Therefore, it is extremely desirable to heal these defects to fabricate high-quality perovskite layers and prolong the moisture-stability of PSCs.

Lots of efforts have been made to improve the crystallinity of perovskite polycrystalline film and minimize the total area of grain boundaries, or to regulate the energy level alignment between perovskite and electron/hole transporting layers to reduce the probability of carriers trapping by defects at the surface, using a variety of approaches including compositional engineering [22-24], interface engineering [25-27], solvent engineering [28] and additive engineering [29, 30]. Among these techniques, the additive engineering is the most popular strategy. Different additives have been reported, such as solvents, fullerene, polymers, organic halide salts, metal halide salts, inorganic acids, and nanoparticles [31-35]. Among these materials, the electron acceptor molecules are usually considered to be effective surface and ionic defects passivation agents, due to their high ionic conductivity, electro-chemical stability and high resistivity against moisture [20, 36]. Recently, it has been proved that the non-fullerene acceptors have shown advantageous impact on the device performance in organic photovoltaic technology by improving especially short current density (J_{SC}) and open circuit voltage (V_{OC}) [37-40]. Along with high quality perovskite film, the performance of PSCs also depends on efficient charge carrier extraction at the interface. Enormous efforts have been made in searching effective buffer layers for transporting photo-generated charge carries efficiently. In those previous reports, an intensely thin film of various materials (BCP, LiF, Ca, ZrAcac, etc.) was usually employed as buffer layer in the devices [25, 41]. However, limited work is performed with a comprehensive study to understand the roles of incorporated molecules and suitable buffer layer on the performance, as well as, moisture-stability of the $MAPbI_3$ based devices.

In this study, we have reported the role of the small molecule IT-4F (3,9-bis(2-methylene-((3-(1,1-dicyanomethylene)-6,7-difluoro)-indanone))-5,5,11,11-tetrakis(4-hexylphenyl)-dithieno[2,3-d:2',3'-d']-s-indaceno[1,2-b:5,6-b']dithiophene) additive to passivate the perovskite

layer in order to fabricate highly efficient and anti-moisture $MAPbI_3$ based PSCs. IT-4F is the novel material related to the family of organic non-fullerene electron acceptors. The optimized ratio of IT-4F incorporation into the perovskite precursor improves the crystallinity, enlarges the grain sizes, successfully reduces the trap density and enhances the charge carrier lifetime for the perovskite film. Based on the optimum ratio modification, the achieved $MAPbI_3$-based planer device exhibits significantly improved PCE from 16.30% to 20.55% with effectively lowest hysteresis. This results from the enhancement of device parameters, especially V_{OC} from 1.10 to 1.16 V for the corresponding devices. Precisely, we have also systematically reported the positive function of the newly used PFN-Br as a thin buffer layer between $PC_{61}BM$ and Ag electrode. This strategy can also prolong the stability of PCSs by making anti-moisture perovskite film, as it is observed by direct water perovskite film interaction. The modified device with IT-4F retains its 80% PCE from its initial value compared to the control device, which retains only about 40% PCE after storage for 30 days in ambient environment. These findings highlight the importance of acceptor molecules interaction with perovskite precursor for improving both efficiency and stability of PSCs.

Result and Discussion

The planar heterojunction PSCs in this research are shown in Figure 1a. The hole transport layer (HTL) employs a 5% Cu doping NiO_x film, which shows excellent hole transport and defect passivation capability [42]. The active layers of $MAPbI_3$ with an additive of novel small molecule IT-4F were fabricated using one step spin coating anti-solvent method [28]. In order to collect the photo-generated electrons in the active layer efficiently, we purposely insert a thin layer of PFN-Br between $PC_{61}BM$ and Ag cathode. The corresponding molecular structures of IT-4F and PFN-

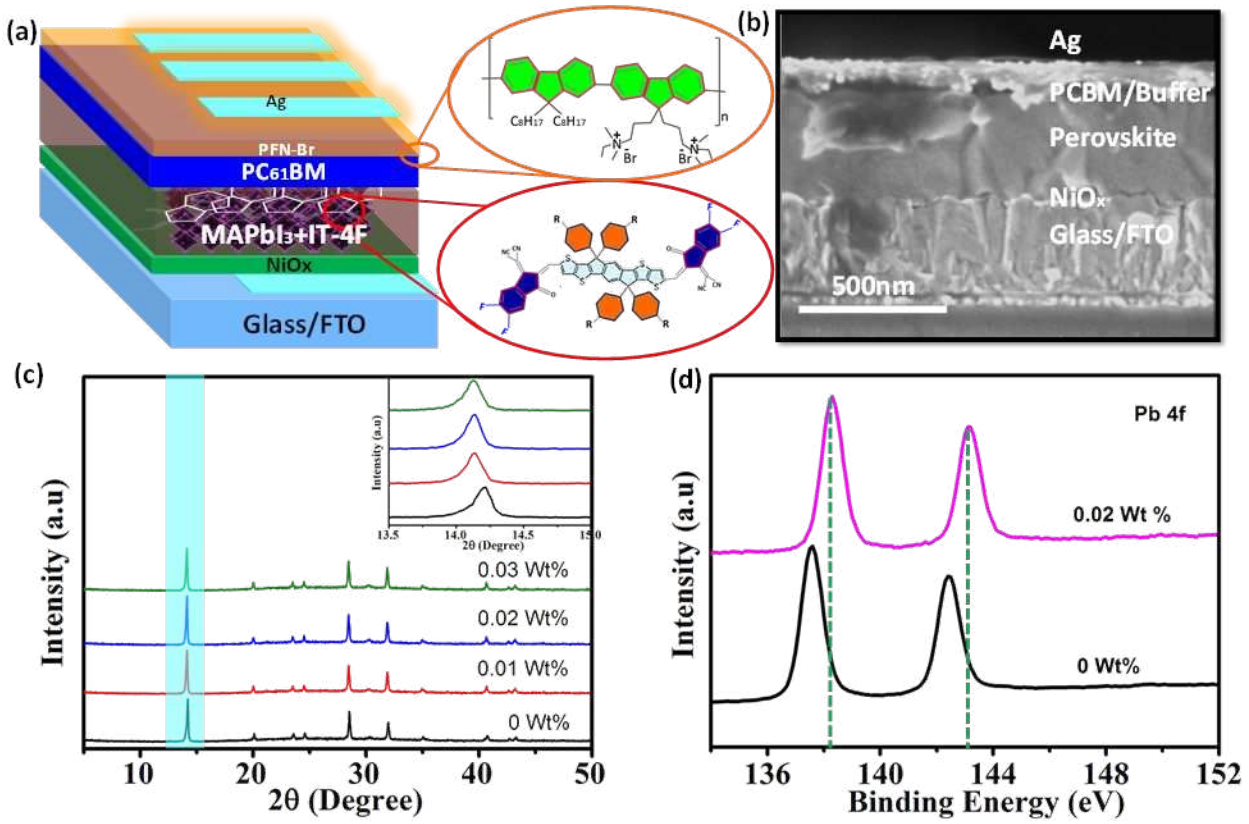

Figure 1. (a) Schematic representation of the adopted device structure. (b) Corresponding cross sectional SEM image of prepared device. (c) XRD spectra of perovskite films with different ratios of IT-4F (inset shows the (001) peak shifting). (d) XPS spectra of Pb 4f region for the perovskite film made with/without IT-4F.

Br is presented in the inset of Figure 1a. The cross-section scanning electron microscopic (SEM) image of the optimized device is shown in Figure 1b. All the functional layers can be apparently distinguished, and closely packed perovskite crystals with a thickness of about 400 nm could be observed. To get a physical insight into the effect of IT-4F on perovskite film growth and crystallization, we have carried out the X-ray Diffraction (XRD) characterization. For convenience, the corresponding perovskite precursors, films or devices containing various IT-4F ratios are defined as "0 Wt%, 0.01 Wt%, 0.02 Wt%, 0.03 Wt% + precursor/film/device or sample",

respectively. Figure 1c indicates the XRD spectra of $CH_3NH_3PbI_3$ film with 0, 0.01, 0.02 and 0.03 Wt% of IT-4F respectively. All the films exhibit strong diffraction peaks at 14.3°, 28.5°, and 32.1°, corresponding to the (110), (220), and (310) lattice planes of the perovskite structure, respectively [43]. This indicates that the incorporation of IT-4F into perovskite precursor does not change the perovskite crystal structure. It is interesting to note that, with increasing the concentration of IT-4F from 0 to 0.02 Wt%, the intensity of (110) diffraction peak strengthens, suggesting the improvement in perovskite crystallinity (Figure S1). With further increasing the concentration of IT-4F to 0.03 Wt%, the corresponding peak intensity dramatically decreases. According to the zoom-in peak of (110) crystallographic plane illustrated in the inset of Figure 1c, the IT-4F incorporation leads to a blue-shifted XRD peak, suggesting an expanded lattice by the presence of the small molecule [36, 44]. As IT-4F molecule having four fluorine atoms located at the corner, thus it is speculated that the interaction of miss-matched ionic radii of fluorine (Fluorine atom is present in the perovskite film as proved by the XPS result as given below) and iodine are responsible for lattice volume expansion, which in turn present blue-shifting of lattice plane [36]. To further explore the interaction of IT-4F with the $CH_3NH_3PbI_3$, we have carried out Fourier transform infrared spectroscopy (FTIR) as shown in Figure S2. A stretching vibration of cyano (C≡N) group can be observed at about 2210 cm^{-1} for the $CH_3NH_3PbI_3$+IT-4F, indicating that IT-4F successfully interacts with the uncoordinated Pb ions [45-47]. Furthermore, a stretching vibration at 1550 cm^{-1}, which can be assigned to the typical C=N vibration [48], was observed in the IT-4F incorporated $CH_3NH_3PbI_3$ sample. These results show that the IT-4F additive remained and chemically interacted with the perovskite film. The perovskite films spin-coated from precursor solution without or with IT-4F were further examined by X-ray photoelectron spectroscopy (XPS) to confirm the role of IT-4F in perovskite films. The XPS spectra in the Pb 4f region for 0 and 0.02

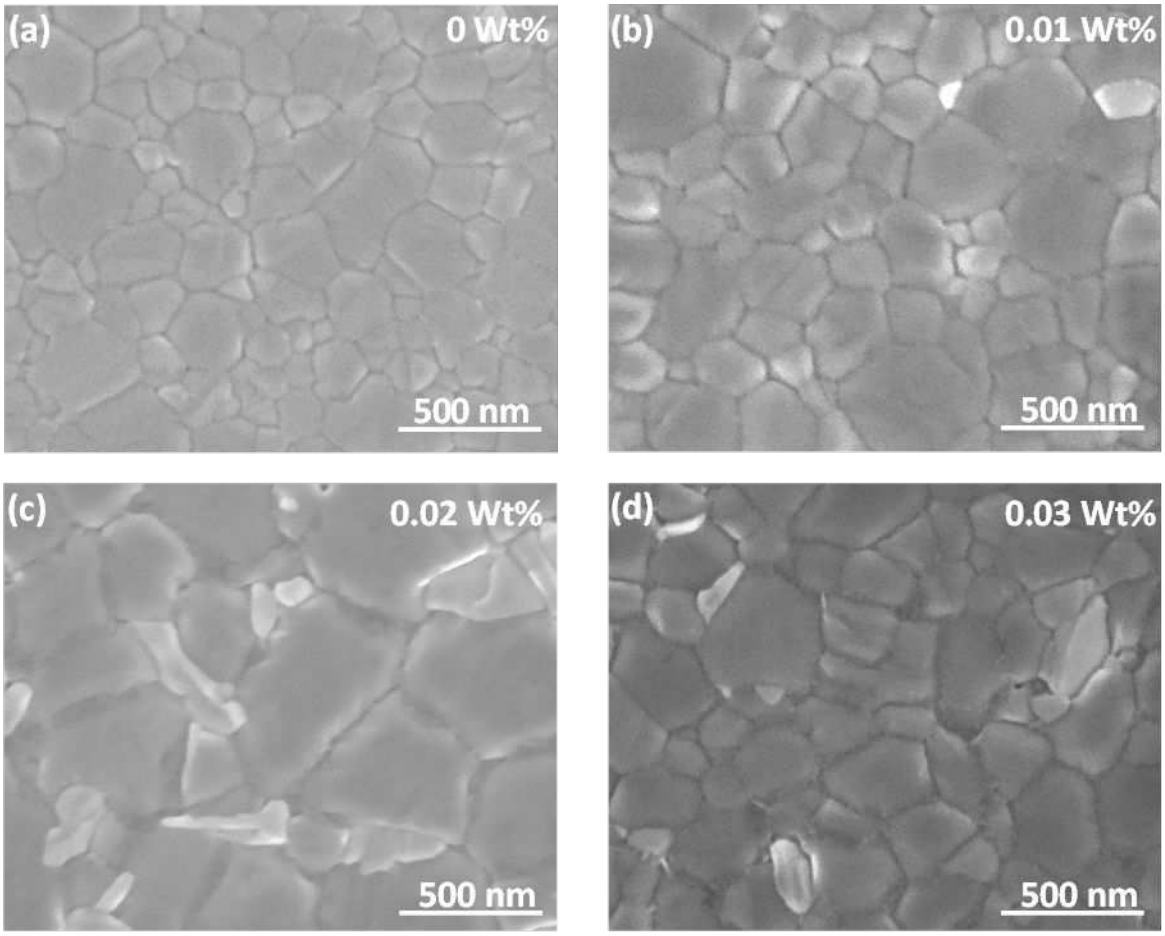

Figure 2. SEM planer view of perovskite films with different Wt% of IT-4F (a) Control or 0 Wt%, (b) 0.01 Wt%, (c) 0.02 Wt%, and (d) 0.03 Wt%.

Wt% IT-4F films are shown in Figure 1d and the corresponding over-all spectra are given in Figure S3a. For the 0 Wt% film, the Pb 4f spectrum exhibits two main peaks at 137.5 and 142.4 eV, corresponding to the Pb $4f_{7/2}$ and Pb $4f_{5/2}$ binding energies, respectively. Whereas, for the 0.02 Wt% film, both Pb $4f_{7/2}$ and Pb $4f_{5/2}$ binding energies shift to higher values, suggesting the existence of chemical interaction between IT-4F and Pb in the perovskite film [49, 50]. A Similar tendency was also observed for C 1s core level spectra as shown in Figure S3b [50]. Further, the F 1s spectra of the 0.02 Wt% film exhibit an apparent peak at 688 eV, as shown in Figure S3c, indicating that IT-4F is successfully incorporated into the perovskite film. To investigate the

influence of IT-4F incorporation strategy on morphology of the perovskite film, the planner-view SEM measurement was carried out. Figure 2a–d give the SEM images of the corresponding $CH_3NH_3PbI_3$ film (0 Wt%) and the films doped by 0.01, 0.02, and 0.03 Wt% IT-4F and the relative grain size distribution is given in Figure S4. Figure 2a shows that the crystal grains of the 0 Wt% film are ordinarily small in the average size of 250 nm and with a large number of grain boundaries. After the small amount of IT-4F incorporation (0.01 Wt%), however, the improved uniform morphology with larger crystal grains has been obtained (Figure 2b), in comparison with the 0 Wt% film. Surprisingly, with further increasing the concentration of IT-4F to 0.02 Wt%, the morphology of the perovskite film further improves, showing an enlarged grain size of more than 500 nm (Figure 2c). Overloading the IT-4F (0.03 Wt%) results in the interruption of perovskite crystallization. Small-size grains with a large number of grain boundaries and few pinholes begin to develop on the surface of perovskite film (Figure 2d). These results suggest that this optimized ratio of IT-4F treatment can effectively promote the crystallization of the perovskite film, which is helpful for inhibiting the recombination process of photo-excited exciton. For further confirming the interaction of IT-4F with perovskite material, we have carried out the high-resolution transmission electron microscopy (HRTEM) elemental mapping as shown in Figure S5. These images clearly indicate the uniform distribution of all the elements in corresponding perovskite film.

As the charge transport mainly depends on the energy level alignment of multiple layers of PSCs, we have employed ultraviolet photoelectron spectroscopy (UPS) (Figure S6) and UV-visible absorption (Figure S7) measurements to calculate the conduction band maximum (CBM) and valence band minimum (VBM) of perovskite film. Interestingly, the perovskite film treated with the optimized ratio of IT-4F (i.e. 0.02 Wt%) shows a good alignment with the respective electron

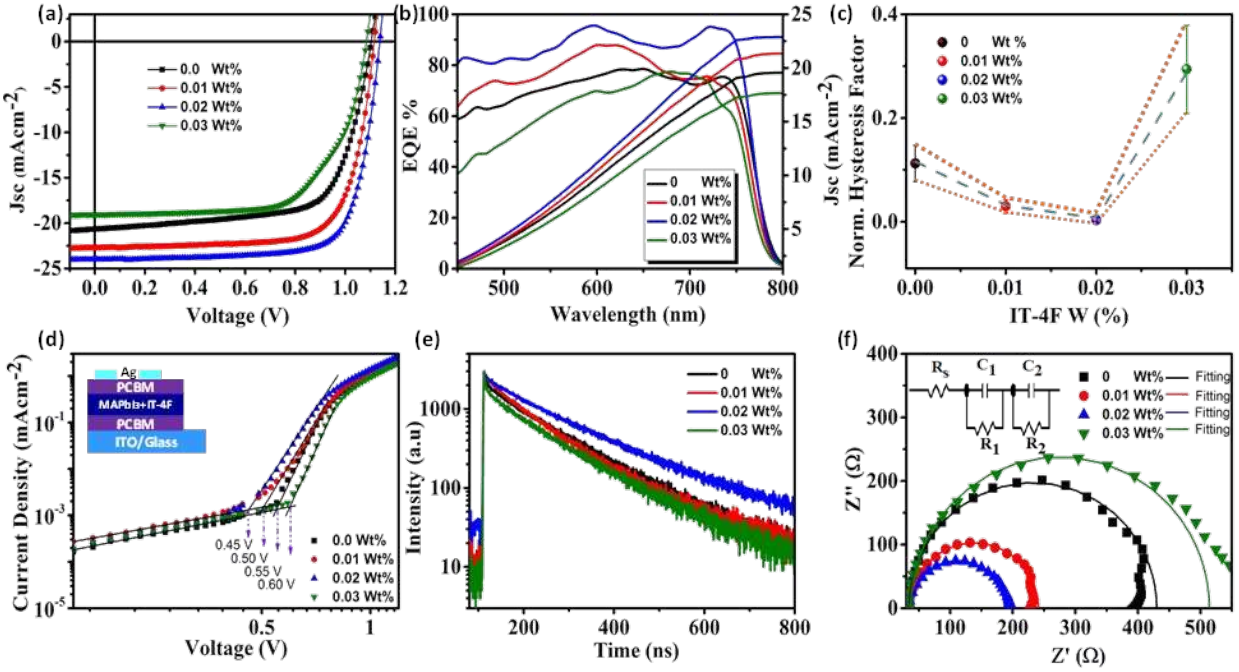

Figure 3. (a) J–V curves of the devices based on 0, 0.01, 0.02, and 0.03 Wt% IT-4F + $MAPbI_3$ perovskite precursor. (b) IPCE and the corresponding integrated J_{SC} spectra of the respective devices. (c) Statistical representation Hysteresis factor as the function of IT-4F ratios in perovskite precursor. (d) Dark J–V curves of the electron only devices with the structure of ITO/$PC_{61}BM$ /perovskite+IT-4F/$PC_{61}BM$/Ag (inset shows the corresponding device structure). (e) TRPL spectra of perovskite films with (0-0.03 Wt%) of IT-4F. (f) Nyquist plots of the Corresponding devices measured in the dark at $V \approx V_{OC}$ (Inset shows the fitting equivalent circuit model).

and hole transport layers compared to that of 0, 0.01 and 0.03 Wt% incorporated films, as shown in Figure S8a. This alignment indicates an energetically favorable transferring of photogenerated charge carriers from the perovskite to the respective transporting layer (Figure S8b). To further examine the influence of IT-4F on the device photovoltaic performance, we fabricated the PSCs with an inverted planar structure and the corresponding energy level alignment of the best performing device (with 0.02 Wt%) is shown in Figure S8b. The current density-voltage (J–V) curves of the set of prepared devices examined under the illumination of AM1.5G 100 mW cm^{-2}

are shown in Figure 3a and the corresponding device parameters are given in Table 1. The 0 Wt% device yields device parameters J_{SC}, V_{OC}, FF and PCE of 20±0.6 mA cm^{-2}, 1.09±0.01 V, 70±2%, and 15.07±1.6% respectively. Interestingly, after 0.01 Wt% IT-4F treatment, the photovoltaic performances of the devices are dramatically improved with PCE of 17.56±1.5%. Further increasing the concentration of IT-4F to 0.02 Wt%, the corresponding devices exhibit enormous improvement of PCE to 20.31±0.21% with J_{SC} of 23.71±0.3 mA cm^{-2}, V_{OC} of 1.14±0.02 V and FF of 76±1%. This efficient device performance could be assigned to the improvement in device parameters, especially in the J_{SC} and V_{OC}, which are enhanced from 20.6 to 23.71 mA cm^{-2} and from 1.08 V to maximum 1.16 V for 0 and 0.02 Wt%, respectively. We have fabricated 10 devices for each condition and the corresponding statistical analysis of J_{SC}, FF, V_{OC} and PCE as the function of IT-4F Wt% ratio is shown in Figure S9. The electron acceptor molecules are usually considered to be effective surface and ionic defects passivation agents, due to their high ionic conductivity and electro-chemical stability [20]. In organic photovoltaic technology, the IT-4F has shown a positive impact on the conductivity of active layer and improved the charge transfer to the electrode, which enhanced the current density remarkably [40]. In our study, the optimized ratio of IT-4F (0.02 Wt%) in the perovskite film not only increases the conductivity of the film but also decreases the series resistance (Rs) of whole device (as given below). Therefore, the improvement in conductivity and decrement in series resistance is the basic reason for the enhancement in current density. This increment in V_{OC} can be attributed to the improvement of the crystallinity, highly uniform film with larger grain sizes and fewer surface defects of optimized (0.02 Wt%) IT-4F-treated $CH_3NH_3PbI_3$ films [36]. This is proved by leakage current measurements of corresponding devices, as shown in Figure S10. However, overloading the IT-4F to 0.03 Wt%, the device performance deteriorated, which could be assigned to the poor morphology of corresponding film.

Table 1. Device parameters based on 0, 0.01, 0.02 and 0.03 Wt% IT-4F incorporated perovskite material.

Ratio of IT-4F [Wt%]	J_{SC} [mA cm^{-2}]	V_{OC} [V]	FF [%]	PCE [%]	J_{SC} (From IPCE) [mA cm^{-2}]
0	20.00±0.6	1.09±0.01	70±2	15.07±1.60	19.52
0.01	21.43±1.3	1.11±0.01	72±1	17.56±1.50	21.30
0.02	23.71±0.3	1.14±0.02	76±1	20.31±0.21	22.85
0.03	18.30±1.0	1.08±0.01	61±4	12.71±1.60	17.66

Figure 3b depicts the incident photon to current efficiency (IPCE) spectra for the respective devices, the integrated current densities were calculated as 19.52, 21.30, 22.85 and 17.66 mA cm^{-2} for the 0, 0.01, 0.02 and 0.03 Wt% IT-4F doped devices, respectively, in good agreement with the J_{SC} obtained from J-V characteristics with a deviation < 1%.

Along with the efficient device performance, the common hysteresis behavior should be low enough for commercial applications. We have fabricated 20 devices with 5 for each condition (i.e. 0-0.03 Wt % of IT-4F) to regulate the hysteresis and the corresponding measured arithmetic mean of hysteresis index (HI) (HI = (PCE_{RS} - PCE_{FS})/PCE_{RS}) [51] is shown in Figure 3c. The relative J-V curves and device parameters measured under forward and reverse scan direction at a scan rate of 10 mV s^{-1} with auto decay interval, are given in Figure S11 and Table S1 respectively. The smaller the value of HI indicates the less hysteresis effect in the device. Interestingly, the device with the optimized ratio of IT-4F (0.02 Wt %) presents remarkably reduced hysteresis compared to the other devices, and the corresponding average values of HI are 0.112, 0.029, 0.0037 and 0.294 for 0, 0.01, 0.02 and 0.03 Wt% IT-4F incorporated devices respectively. Previously, it has been proved that the native defects or trap states on the surface of active layer are responsible for charge

carrier's non-radiative recombination, and result in notorious hysteresis [33, 52]. The efficient device performance with lower hysteresis should be attributed to the passivation of trap state by a precise amount of IT-4F incorporation into perovskite precursor. To evidence this, we have calculated the trap state density (n_t) by using space charge limited current (SCLC) strategy [53] (further detail is added in Section 1 in supporting information),

$$n_t = \frac{2\varepsilon\varepsilon_o V_{TFL}}{qL^2} \quad (1)$$

where V_{TFL}, L, ε and ε_o are the trap filled limited voltage, the thickness of the perovskite film, the relative dielectric constant (for $MAPbI_3$ taken as 25.7 [54]) and the vacuum permittivity, respectively. Figure 3d shows the dark J-V characteristics of electron only device with configuration of ITO/$PC_{61}BM$/$CH_3NH_3PbI_3$+IT-4F(0-0.03Wt%)/$PC_{61}BM$/Ag (inset Figure 3d). It is observed that the n_t significantly decreases from 0.58 to 0.47 x 10^{10} cm^{-3} for the 0.00 and 0.02 Wt% IT-4F passivated devices respectively (Table S2), suggesting the IT-4F effectively passivates the native defects in perovskite film. To further clarify our results, we have also calculated the Hall mobility, resistivity and carrier concentration as the function of different weight ratios of IT-4F by employing Hall Effect measurements, as shown in Figure S12. The hole mobility and carrier concentration remarkably increased from 199 to 277 cm $V^{-1}s^{-1}$ and 1.33 to 4.37 x 10^5 cm^{-2} for the 0.00 and 0.02 Wt% IT-4F treated films respectively, in agreement with our trap density results. On the other hand, the resistivity significantly decreases to 0.198 from 2.04 x 10^{11} Ω cm by the incorporation of the optimized ratio of IT-4F. We believe that the decrement in resistivity could be assigned to the reduced defects and increased charge conductivity with the incorporation of IT-4F molecule. As shown in Figure S13, the 0.02 Wt% IT-4F incorporated perovskite film has better conductivity than the 0, 0.01 and 0.03 Wt% IT-4F films, which demonstrates the fast carriers transport in the optimized concentration of IT-4F incorporated perovskite films.

Time-resolved photoluminescence (TRPL) measurements were carried out to further clarify recombination behaviors of photoexcited carriers in the perovskite film. The TRPL spectra of $MAPbI_3$ + (0-0.03 Wt%) IT-4F films spin-coated on glass are shown in Figure 3e and the corresponding steady state spectra are given in Figure S14. The obtained result indicates a much higher carrier's lifetime for the 0.02 Wt% film, compared with the 0.00 Wt%, 0.01 Wt%, and 0.03 Wt% films as shown in Table S3. As well known, the improved charge carrier lifetime is the indication of lower surface defects or trap states and less non-radiative recombination suggests that the optimized ratio of IT-4F incorporation produces high quality crystals with fewer grain boundaries as proved by XRD and SEM results. As a result, we believe that the reduction in hysteresis in the champion ratio is corresponding to the reduction in trap density and non-radiation recombination, which is well consistent with our respective measurements. To get direct evidence of charge transport mechanism, we have calculated the charge transfer resistance by employing impedance spectroscopy, as shown in Figure 3f. Nyquist plots of the devices with different IT-4F ratios were measured and the corresponding resistance values are tabulated in Table S4. The diameter of Nyquist plot is directly related to the charge transfer resistance. The 0.02 Wt% IT-4F device presents the smallest semicircle, suggesting that the charge transport resistance is remarkably lower compared to that of other devices. This result indicates that the optimized IT-4F ratio is promoting the charge transport to the electrodes and improving the FF of the device (the corresponding comparison between FF and series resistance (R_s) is shown in the Figure S15), which is helpful for efficient device performance.

Figure 4 shows the positive function of PFN-Br, which is purposely inserted as buffer layer between $PC_{61}BM$ and Ag electrode. Figure 4a shows the TRPL spectra of structures based on ITO/$CH_3NH_3PbI_3$, ITO/$CH_3NH_3PbI_3$ + (0.02 Wt%) IT-4F/$PC_{61}BM$ and ITO/$CH_3NH_3PbI_3$+(0.02

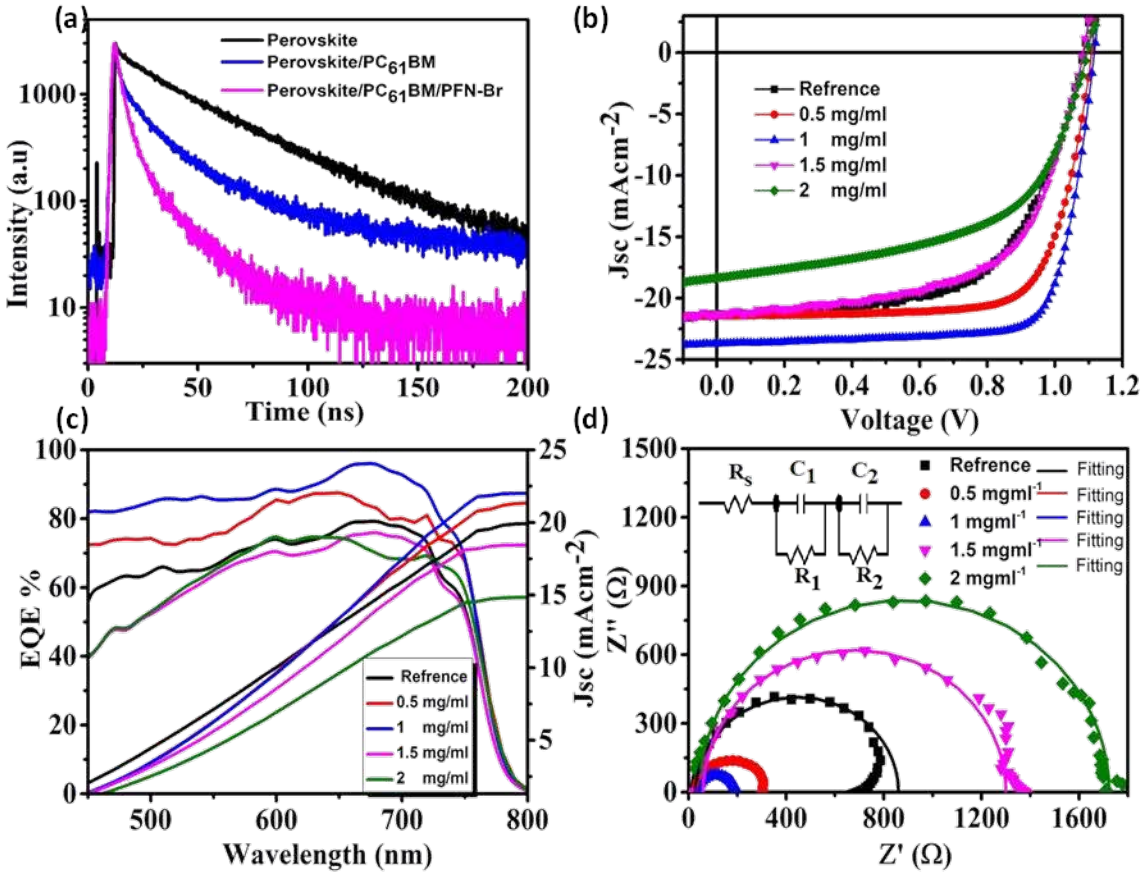

Figure 4. (a) TRPL measurements of perovskite/glass, PCBM/Perovskite/glass and PFN-Br/ PCBM/Perovskite/glass films. (b) J-V characteristics of PSCs with (0-2 mg mL^{-1}) PFN-Br buffer layer modification. (c) The IPCE spectra of the corresponding devices. (d) Nyquist plots of the corresponding devices with different PFN-Br concentration modification (inset shows the corresponding fitting equivalent circuit model).

Wt%) IT-4F/$PC_{61}BM$/PFN-Br structures. Interestingly, the structure spin-coated with the optimized concentration of PFN-Br shows a fast decay than the one without modification, suggesting that the presence of PFN-Br could stimulate the transport of electrons to the electrode. Figure S16 shows the steady state PL spectra of the corresponding films. It can be seen that the PL intensity of PFN-Br modified film is much suppressed compared to its counterpart, indicating the efficient electron transfer before recombination. These results are attributed to the fact that the

PFN-Br modification can promote the separation of charge carriers and reduce the process of radiative recombination in the optimized devices [55]. Figure 4b presents the J-V characteristics of the series of device with different concentrations of PFN-Br modification on ETL and the corresponding device parameters are given in Table 2. The control device without any modification presents a J_{SC} of 20.0±1.3 mA cm^{-2}, a V_{OC} of 1.1±0.01 V, FF of 65±3% and PCE of 13.03±1.2%, which is comparable to the previously reported results [56]. Additionally, we have also calculated the HI of fabricated devices with different ratios of PFN-Br as shown in Figure S17. To examine the role of PFN-Br modification, the buffer layers were fabricated with various concentrations of the methanol stock solutions. With the enhancement in concentration from 0 to 1 mg mL^{-1}, the device presents an improvement in performance. This presents that the existence of PFN-Br does certainly enhance the device efficiency with suppressed hysteresis (Figure S17). However, the thickness should not be too large due to its insulating nature. When the PFN-Br film thickness further increased by overloading its concentration (1.5 and 2 mg mL^{-1}), the device performance deteriorates, especially in FF and the corresponding statistical values are shown in Figure S18. These results indicate that the PFN-Br modification at the interface, positively contributes to the performance by reducing the probability of electron trapping between $PC_{61}BM$ and Ag, presenting similar functionality of BCP [56]. To get more information, the IPCE measurements of corresponding devices were carried out as shown in Figure 4c. The devices based on the optimized ratio of PFN-Br, exhibits broad spectrum and high IPCE values, suggesting efficient ability for transforming solar energy to electricity for the respective devices. The integrated J_{SC} values calculated from the IPCE spectra are 19.94, 21.35, 22.01, 18.45 and 14.87 mA cm^{-2} for 0 to 2 mg mL^{-1} PFN-Br concentrations, respectively. These values are well in agreement with the J_{SC} obtained from J-V characteristics within a deviation of about 1.5%.

Table 2. Device parameters based on 0, 0.5, 1, 1.5 and 2 mg mL^{-1} PFN-Br buffer layer.

Ratio of PFN-Br mg mL^{-1}	J_{SC} [mA cm^{-2}]	V_{OC} [V]	FF [%]	PCE [%]	J_{SC} (From IPCE) [mA cm^{-2}]
0	20.0±1.30	1.1±0.01	65.0±3	13.03±1.20	19.94
0.5	20.5±0.83	1.11±0.01	72.8±1	16.56±1.00	21.35
1	23.7±0.31	1.13±0.01	76.0±1	20.31±0.21	22.01
1.5	20.0±1.50	1.09±0.01	61.0±4	13.71±1.60	18.45
2	18.5±1.5	1.08±0.01	55±2	8.6±2	14.87

By employing the SCLC technique on the single carrier (electron-only) device, the electron mobility of the devices with various concentrations of PFN-Br was examined. The $J^{1/2}$–V curves of the series of electron only devices with different concentrations of PFN-Br fitted with the Mott–Gurney law [3] are shown in Figure S19a. The device modified with 1 mg mL^{-1} PFN-Br solution, presents high electron mobility, 4.30 x 10^{-4} $cm^{-2}v^{-1}s^{-1}$, which is about 3-fold larger than the reference device (Table S5). Whereas, other ratios of PFN-Br (0.5 and 2 mg mL^{-1}) also deteriorate the electron mobility. In addition, the electron trap-state density of the same electron-only devices was also calculated using dark J-V curves as shown in Figure S19b and the corresponding n_t and V_{TFL} values are given in Table S6. The trap density is remarkably reduced from 0.55 x 10^{10} cm^{-3} for the control device to 0.29 x 10^{10} cm^{-3} for the PFN-Br 1 mg mL^{-1} modified device. For a higher concentration of the PFN-Br modification, trap density is even higher than that of the control one, which leads to higher charge recombination at the interface, particularly resulting in FF deterioration [42]. To further evidence to the origin of the improved FF along with enhanced J_{SC}, we quantitatively calculated the charge transfer resistance of fabricated devices with different PFN-

Br modifications using impedance spectroscopy technique. Figure 4f shows the Nyquist plots of devices with different ratios of PFN-Br and the corresponding fitted resistance values are given in Table S7 and the comparison between FF and R_s as the function of PFN-Br is given in the Figure S20. The devices with the optimized PFN-Br modification indicate a decrement in the diameter of the semicircles as the mass ratio gradually enhances from 0 to 1 mg mL^{-1}. Whereas, the diameter increases as the concentration is overloaded to 2 mg mL^{-1}. This illustrates that the precise amount of PFN-Br could effectively promote electron transfer, leading to superior device performance.

The stability of perovskite material in humid environment is a huge hurdle in commercialization of this photovoltaic technology. It is an obvious fact that the hybrid perovskites are extremely perceptive to moisture [57]. Previously, it has been reported that the moisture induces degradation of polycrystalline perovskite film initiated at the grain boundaries. Hence the highly uniform perovskite surface with less grain boundaries plays a very important role in moisture stability of the PSCs [58, 59]. Typically, large crystal grains with effective passivation at grains boundaries can block the surface initiated disintegration of perovskite structure and hence extensively increase their ambient environmental stability. Here, we examined the impact of passivation on moisture-stability of perovskite film by water drop casting on the films in ambient environment as illustrated in Figure 5a-f. First, we spin-coated the control and doped perovskite films under the same conditions in N_2 glove box. Then, we took them out and dropped the equal volume of water on the corresponding films (Figure 5a). On drop casting, the pristine $CH_3NH_3PbI_3$ film quickly reacts with water and decomposes from black perovskite phase to yellowish PbI_2 (Figure 5b), δ-phase is an intermediate state [33]. With the passage of time, the water molecule decomposes the whole perovskite film and spread all over the surface within one hour as shown in Figure 5c-f. On the other hand, the $CH_3NH_3PbI_3$ film passivated by IT-4F presents a remarkably higher resistance

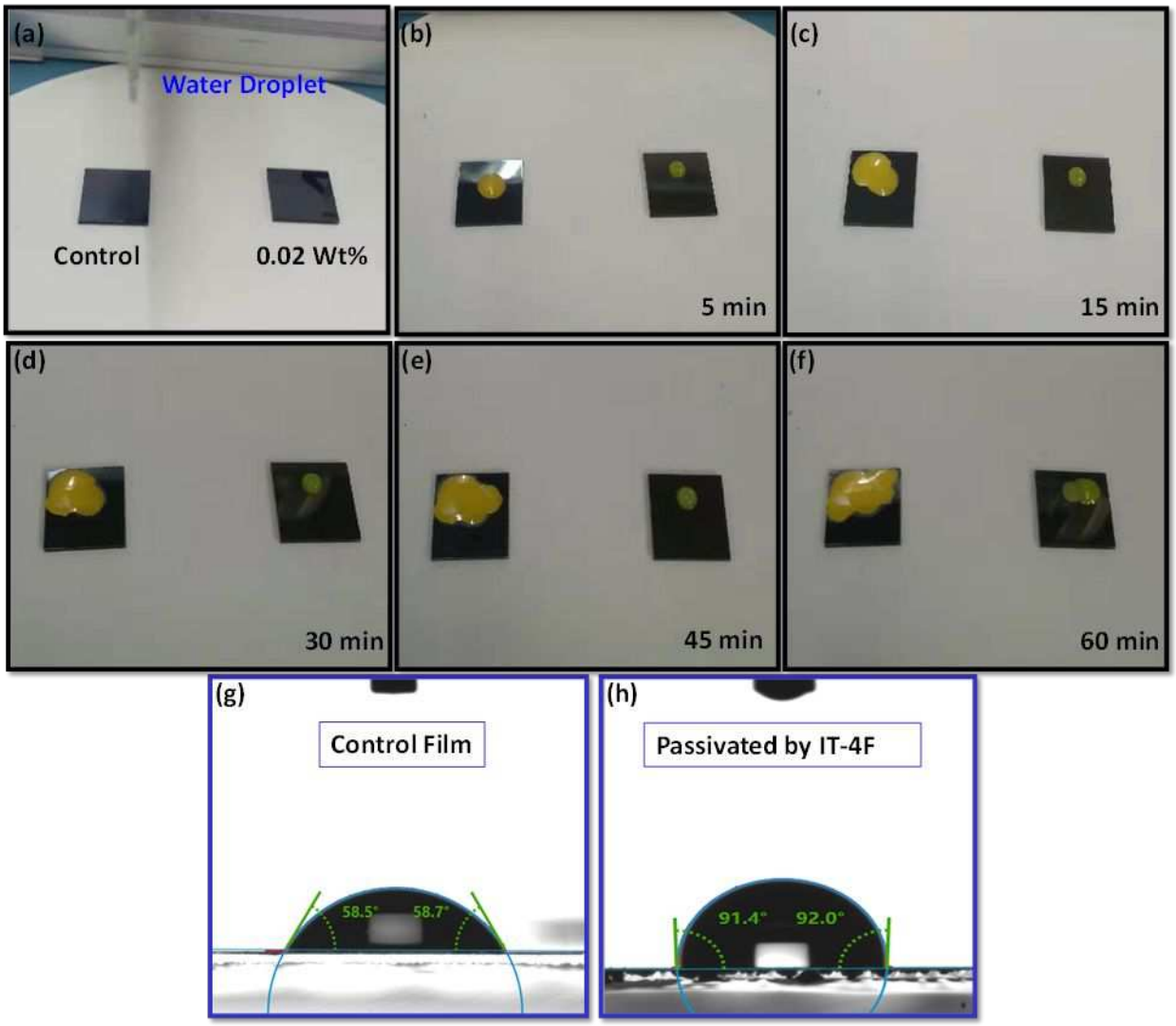

Figure 5: (a) Water droplet interacts with control and doped perovskite films (a) 0 min interaction (b) 5 min (c) 15 min (d) 30 min of interaction (e) 45 min (f) 60 min. Water contact angle measurements of (g) control and (h) IT-4F passivated perovskite films.

against perovskite degradation by water molecule. Intriguingly, the doped films are unexpectedly stable in such water-perovskite interaction, with little expansion of water over the surface after 1 h of concentrated liquid invasion (Figure 5f). These results suggest that the passivation by IT-4F positively could realize moisture resistive perovskite films for highly humid environment stable devices. To clarify the improvement of moisture-stability, we propose the possible mechanism:

the IT-4F passivated perovskite layer presents a good hydrophobic behavior, thus preventing the possible moisture penetration into perovskite. To proof it, we have conducted the water contact-angle measurement for corresponding films as shown in Figure 5g-h. Interestingly, the perovskite film treated with IT-4F presents a larger contact-angle of 92° compared to the control perovskite film with a small contact-angle of 58°. The large difference of contact-angle among the two samples indicates that the IT-4F incorporation makes the $CH_3NH_3PbI_3$ film hydrophobic. Therefore, the considerable contribution of IT-4F passivation on the enhancement of moisture-stability should be from the reduced water reactivity with perovskite surface.

As discussed above, the IT-4F incorporation into perovskite precursor can not only improve the device performance, but also present hydrophobic capability for $MAPbI_3$ perovskite film. Therefore, the IT-4F incorporation can be anticipated to increase the long-term stability of PSCs, particularly in a high humid environment. Therefore, we record the deviation in PCE of the un-encapsulated devices placed in ambient conditions with a RH of 10-30% at room temperature. The normalized PCE values measured after various time intervals for 30 days are shown in Figure 6a and the corresponding device parameters are given in Figure S21. The PCE of the control device (without IT-4F) rapidly decreases by about 60% of its initial value within 20 days. On the contrary, the IT-4F treated device can successfully maintain about 80% of its initial efficiency even after 30 days storage. Further, we have also conducted the aging test in a highly humid environment for the control and IT-4F incorporated devices (unencapsulated) by storing them into a humidity-controlled chamber with RH of 50, 70 and 90%, shown in the Figure 6b, c, and d respectively. The average PCE of the control devices drops rapidly and maintains about 68, 62 and 27% of its initial efficiency for RH 50, 70, and 90% respectively, under harsh humidity conditions for 1 hour. On the other hand, the IT-4F incorporated devices present remarkable stability under the same

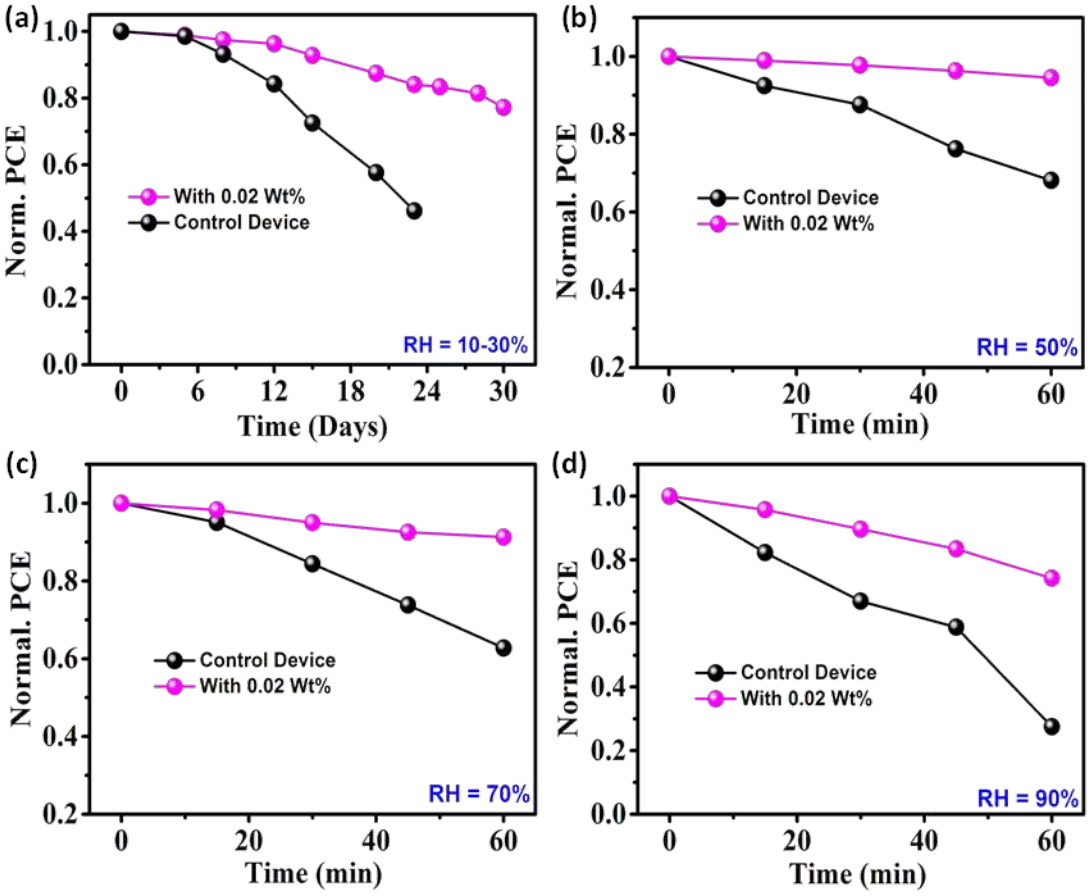

Figure 6. The stability of the control and champion (with 0.02 Wt% of IT-4F and 1 mg/ml PFN-Br) devices stored (a) in ambient environment (RH 10-30%) measured after various time intervals for 30 days. Stability of the corresponding devices stored in humidity chamber with (b) RH = 50% (c) RH = 70% (d) RH = 90% measured with the interval of 15 min for 1 hour.

condition with PCE values maintained about 94, 91 and 74% of its initial efficiency. The exploratory results demonstrate that the IT-4F modified devices show superior device stability, because of its hydrophobic perovskite layer, which could hinder the permeation of moisture. We conclusively confirm that corresponding passivation could improve the moisture stability of organic-inorganic hybrid perovskite films.

To further support our findings of anti-moisture perovskite film using the optimized ratio of IT-4F, we have carried out XRD measurements of respective films under different humidity conditions, which are considered an effective tool to understand the better moisture resistance capability [21]. Figure 7a shows the XRD spectra of control film (without IT-4F) measured at 0, 20 and 40 days aging period in RH = 10-30% at room temperature. It can be seen that there is no PbI_2 peak in the fresh sample, but after 20 days storage a large peak of PbI_2 appears at 12.6° compared to perovskite (110) plane peak, suggesting very poor perovskite phase stability even under low humidity conditions (10-30%). After 40 days storage the perovskite phase (110) disappears, and the film is visibly yellow. In contrast, the modified film with IT-4F clearly presents a strong perovskite phase after 20 days storage under the same conditions, as shown in Figure 7b. However, there is a tiny peak of PbI_2 appears in comparison to the control film, indicating that the IT-4F incorporated film demonstrates a significantly improved perovskite phase stability. After 40 days the perovskite and PbI_2 peak has approximately equivalent signal and the film is not completely visibly yellow. Furthermore, we have also conducted XRD measurements on control (without IT-4F) and doped (with IT-4F) perovskite films barely stored under different humidity environments (with RH = 50, 70, and 90% respectively) for 3 hours, and the corresponding XRD spectra are shown in Figure 7c. It can be observed the IT-4F treated film shows the strong perovskite peak even in a harsh humid environment compared to that of the control film, which presents a strong PbI_2 phase under the same conditions. The degree of perovskite phase disintegration is quantified by the ratio of PbI_2 peaks to perovskite peaks as the function of RH (Figure 7d). The much slower devaluation of the perovskite phase and the slower emergence of the PbI_2 phase in the perovskite films with IT-4F incorporation illustrate the excellent moisture resistance potential enabled by the

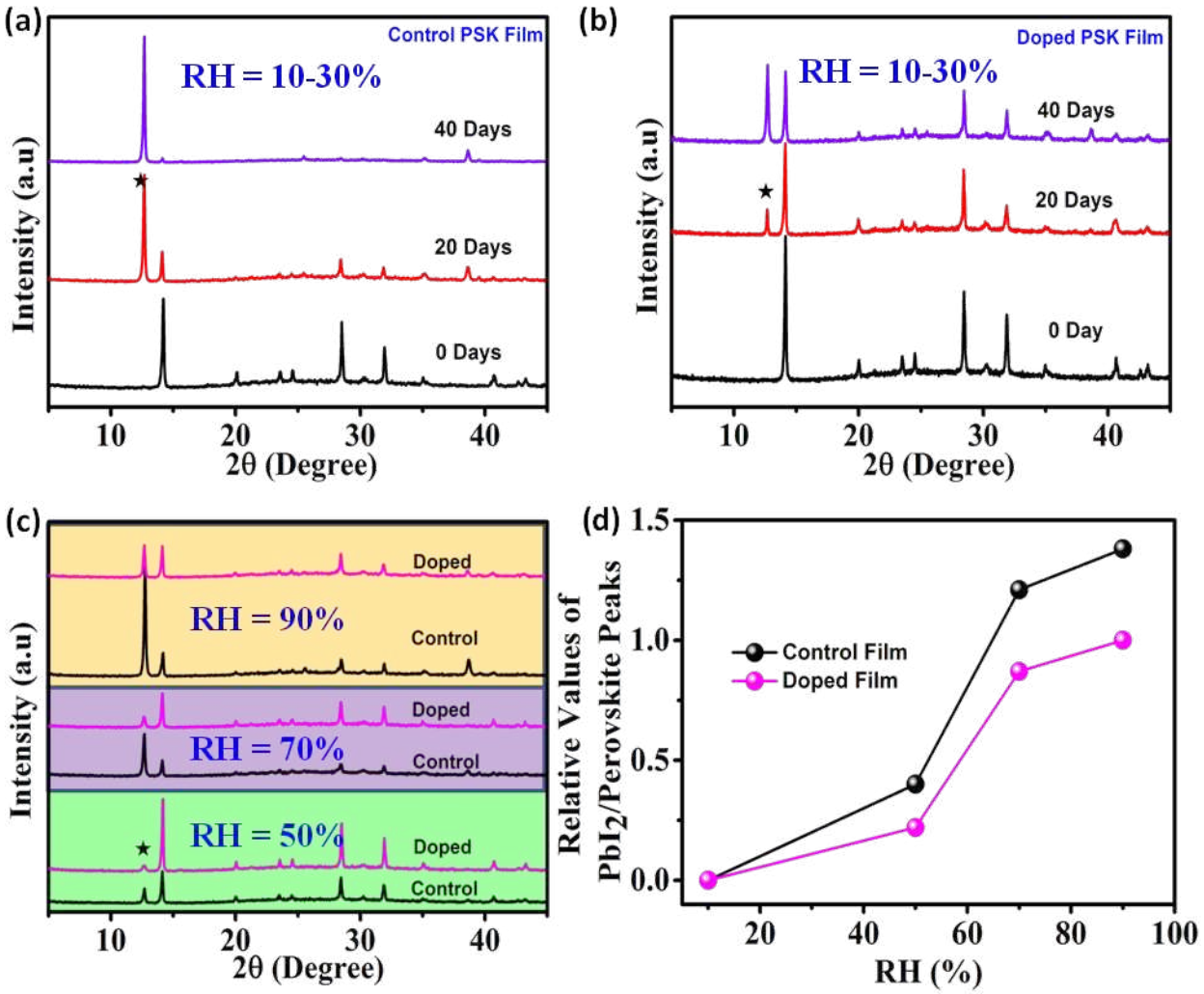

Figure 7: XRD measurements of (a) Control and (b) Doped perovskite film stored under ambient condition (RH = 10-30%) at room temperature. (c) XRD spectra comparison of control and doped perovskite films stored in humidity chamber for 3 hours with RH of 50, 70 and 90% respectively (small star shows the PbI_2 peak). (d) Relative values of PbI_2/perovskite as the function of RH.

surface treatment. These results are well consistent with our water-perovskite interaction observation and respective device stability measurements.

Conclusion

In summary, we have demonstrated that the IT-4F incorporation into $MAPbI_3$ perovskite can successfully improve the photovoltaic performance. The strong interaction of IT-4F to perovskite

results in high quality film with large crystal grains, leading to the prolonged PL lifetime and the reduction in trap density. The optimized ratio of IT-4F regulates the energy level alignment of perovskite film with corresponding electron and hole transport layers, which facilitates the photo-generated charge carriers transport with the minimal recombination at interface. Moreover, the modification at the PCBM/Ag interface by an optimum concentration of PFN-Br buffer layer, promotes the electron extraction by electrode, leading to the improved FF from 72 to 77%. These collective advantages boost PSCs efficiency significantly to 20.55% with reduced hysteresis. Furthermore, the IT-4F incorporated films present extraordinary resistance against moisture by making $MAPbI_3$ film hydrophobic. As a result, the $MAPbI_3$+0.02 Wt% IT-4F based devices also exhibit long term stability by retaining its 80% PCE of its initial value, after aged under ambient environment (RH=10-30%) for 30 days without encapsulation. Our findings fascinate the potential of using small molecules in additive engineering for highly efficient stable PSCs and open the path towards commercialization of this technology.

Experimental Section

Materials: MAI and PbI_2 were purchased from DYESOL and Sigma Aldrich respectively. $PC_{61}BM$ and DMF were obtained from Sigma-Aldrich. Nickel acetate tetrahydrate ($Ni(CH_3COO)_2•4H_2O$) and cupric acetate monohydrate ($Cu(CH_3COO)_2•H_2O$) were got from Sinopharm Chemical Reagent Co. Ltd. IT-4F was obtained from 1-Material. All the solvents were obtained from Beijing Chemical Works. All the corresponding solvents and chemicals were employed as received.

Solution preparation: First, we made solution for HTL, the desired ratio was prepared in anhydrous ethanol (0.1 M) with 6 μl mL^{-1} ethanolamine addition in NiO_x solution. Then we prepared IT-4F solution in chlorobenzene (10 mg mL^{-1}) and stirred it in N_2 glove box for 12 hours at 50 °C. The $MAPbI_3$ perovskite precursor was prepared with 1:1 mole ratio of MAI and PbI_2 with 1.2 M

concentration in anhydrous DMF. Before stirring it, the desired amount of IT-4F was added into $MAPbI_3$ perovskite precursor to make 0.01, 0.02 and 0.03 Wt% IT-4F incorporated solutions and then stirred about 15 hours in glove box at 55 ^oC. For electron extraction from the active layer, (20 mg mL^{-1}) $PC_{61}BM$ was dissolved in chlorobenzene and stirred at 50 ^oC for whole night. Finally, to prepare electron buffer layer, first we dissolved PFN-Br into methanol (20 mg mL^{-1}). Then we made different (0.5, 1, 1.5 and 2 mg mL^{-1}) ratios of PFN-Br.

Device Fabrication: Here we have adopted inverted planer configuration to fabricate the PSCs. First of all we cleaned FTO glasses sequentially with DI water, isopropanol, acetone and ethanol. Then, after 15 min ozone cleaning, HTL was spin coated at 3k rpm with the time interval of 30 s and annealed for 1 h at 340 ^oC. After cooling to 100 ^oC, the samples were taken to N_2 glove box for perovskite layer fabrication. The perovskite layer was fabricated using one step spin coating method, for this 30 µl perovskite precursor was dropped on HTL/FTO substrate and spin-coated at 6000 rpm for 30 s. After desire interval of time, anhydrous toluene was abruptly dropped on the spinning substrate. After waiting about 10 min, the perovskite spin-coated films were transferred to hot-plate for annealing at 100 °C for 10 min. After cooling down to room temperature of active layer, the ETL was spin-coated at 1000 rpm for 30 s using $PC_{61}BM$ solution. For buffer layer PFN-Br was spin-coated on top of the $PC_{61}BM$ layer at 4000 rpm for 30 s. Finally, for cathode Ag metal was evaporated by thermal evaporation under high vacuum and the thickness of Ag electrode was 100 nm.

Characterization: For device testing, the current Density-voltage (J-V) characteristics were performed on Keithley 2450 source measure unit under one sun illumination condition (AM 1.5G, 100 mW cm^{-2}). The XRD spectra were measure employing a Rigaku V2500 X-ray diffractometer. XPS spectra were acquired from Thermo Fisher ESCALAB 250Xi. The SEM images of the

corresponding films/device were obtained from JSM-7401F. UPS measurements were performed on AXIS ULTRA DLD. QEPVSI-B Measurement System (Newport) was employed to obtain IPCE results. UV-vis, Persee TU-1950 spectrophotometer was used to measure Absorbance spectra of respective perovskite films. Hall Effect results were obtained from van der Pauw configuration using Nanomatrics Hall measurement system model HL5500. TRPL results were obtained time correlated single photon counting (TCSPC) system (Edinburgh F900).

ASSOCIATED CONTENT

Supporting Information

The Supporting Information is available free of charge on the ACS Publications website at DOI: SCLC details, UPS spectra, absorbance spectra, Hall Effect measurements, XPS data, TEM results, hysteresis data, dark J-V curves, grain size distribution, photovoltaic data, PL spectra, and supporting tables

Notes

The authors declare no competing financial interest.

AUTHOR INFORMATION

Corresponding Author

* wangzj@semi.ac.cn

* qsc@semi.ac.cn

* yong.lei@tu-ilmenau.de

ACKNOWLEDGMENT

This work was financially supported by the National Key Research and Development Program of China (Grant No. 2017YFA0206600), Key Research Program of Frontier Science, CAS (Grant No. QYZDB-SSW-SLH006), National Natural Science Foundation of China (Contract Nos. 61674141, 51972300, 21975245 and 62011530022), and German Research Foundation (DFG: LE 2249/5-1). The Strategic Priority Research Program of Chinese Academy of Sciences，Grant No. XDB43000000. Z. W. appreciates the support from Hundred-Talent Program (Chinese Academy of Sciences).

REFERENCES

1. Stranks, S. D.; Eperon, G. E.; Grancini, G.; Menelaou, C.; Alcocer, M. J.; Leijtens, T.; Herz, L. M.; Petrozza, A.; Snaith, H. J., Electron-Hole Diffusion Lengths Exceeding 1 Micrometer in an Organometal Trihalide Perovskite Absorber. *Science* **2013,** *342* (6156), 341-344.

2. Xing, G.; Mathews, N.; Sun, S.; Lim, S. S.; Lam, Y. M.; Gratzel, M.; Mhaisalkar, S.; Sum, T. C., Long-Range Balanced Electron- and Hole-Transport Lengths in Organic-Inorganic $CH_3NH_3PbI_3$. *Science* **2013,** *342* (6156), 344-347.

3. Dong, Q.; Fang, Y.; Shao, Y.; Mulligan, P.; Qiu, J.; Cao, L.; Huang, J., Solar Cells. Electron-Hole Diffusion Lengths > 175 μm In Solution-Grown $CH_3NH_3PbI_3$ Single Crystals. *Science* **2015,** *347* (6225), 967-970.

4. Liao, W.-Q.; Tang, Y.-Y.; Li, P.-F.; You, Y.-M.; Xiong, R.-G., Large Piezoelectric Effect in a Lead-Free Molecular Ferroelectric Thin Film. *J. Am. Chem. Soc.* **2017,** *139* (49), 18071- 18077.

5. Green, M. A.; Ho-Baillie, A.; Snaith, H. J., The Emergence of Perovskite Solar Cells. *Nat. Phot.* **2014,** *8* (7), 506-514.

6. Pellet, N.; Gao, P.; Gregori, G.; Yang, T. Y.; Nazeeruddin, M. K.; Maier, J.; Gratzel, M., Mixed-Organic-Cation Perovskite Photovoltaics for Enhanced Solar-Light Harvesting. *Angew Chem. Int. Ed. Engl.* **2014,** *53* (12), 3151-3157.

7. Kojima, A.; Teshima, K.; Shirai, Y.; Miyasaka, T., Organometal Halide Perovskites as Visible-Light Sensitizers for Photovoltaic Cells. *J. Am. Chem. Soc.* **2009,** *131* (17), 6050-6051.

8. Best Research-Cell Efficiencies, National Renewable Energy Laboratory (NREL), https://www.nrel.gov/pv/. (Accessed on May 2020)

9. Yang, W. S.; Park, B.-W.; Jung, E. H.; Jeon, N. J.; Kim, Y. C.; Lee, D. U.; Shin, S. S.; Seo, J.; Kim, E. K.; Noh, J. H.; Seok, S. I., Iodide Management in Formamidinium-Lead-Halide–Based Perovskite Layers lor Efficient Solar Cells. *Science* **2017,** *356* (6345), 1376-1379.

10. Liu, C.; Wang, K.; Du, P.; Yi, C.; Meng, T.; Gong, X., Efficient Solution-Processed Bulk Heterojunction Perovskite Hybrid Solar Cells. *Adv. Energy Mater.* **2015,** *5* (12), 1402024.

11. Azam, M.; Yue, S.; Xu, R.; Liu, K.; Ren, K.; Sun, Y.; Liu, J.; Wang, Z.; Qu, S.; lei, Y.; Wang, Z., Highly Efficient Solar Cells Based on Cl Incorporated Tri-Cation Perovskite Materials. *J. Mater. Chem. A* **2018,** *6* (12), 13725-13734.

12. Wu, Y.; Yang, X.; Chen, W.; Yue, Y.; Cai, M.; Xie, F.; Bi, E.; Islam, A.; Han, L., Perovskite Solar Cells with 18.21% Efficiency and Area Over 1 cm^2 Fabricated by Heterojunction Engineering. *Nat. Energy* **2016,** *1*, No. 16148.

13. Azam, M.; Yue, S.; Liu, K.; Sun, Y.; Liu, J.; Ren, K.; Wang, Z.; Qu, S.; Wang, Z., Insights on the Correlation of Precursor Solution, Morphology of the Active Layer and Performance of the Pervoskite Solar Cells. *J. Alloys Comp.* **2018,** *731*, 375-380.

14. deQuilettes, D. W.; Vorpahl, S. M.; Stranks, S. D.; Nagaoka, H.; Eperon, G. E.; Ziffer, M. E.; Snaith, H. J.; Ginger, D. S., Solar cells. Impact of Microstructure on Local Carrier Lifetime in Perovskite Solar Cells. *Science* **2015,** *348* (6235), 683-686.

15. Shi, D.; Adinolfi, V.; Comin, R.; Yuan, M.; Alarousu, E.; Buin, A.; Chen, Y.; Hoogland, S.; Rothenberger, A.; Katsiev, K.; Losovyj, Y.; Zhang, X.; Dowben, P. A.; Mohammed, O. F.; Sargent, E. H.; Bakr, O. M., Low Trap-State Density and Long Carrier Diffusion in Organolead Trihalide Perovskite Single Crystals. *Science* **2015,** *347* (6221), 519-522.

16. Chao, L.; Dandan, Z.; Yan, L.; Xiaojun, L.; Shaomin, P.; Guosheng, S.; Guichuan, X., Ruddlesden–Popper Perovskite for Stable Solar Cells. *Energy Environ. Mater.* **2018,** *1* (4), 221-231.

17. Chen, J.; Kim, S.-G.; Ren, X.; Jung, H. S.; Park, N.-G., Effect of Bidentate and Tridentate Additives on the Photovoltaic Performance and Stability Of Perovskite Solar Cells. *J. Mate. Chem. A* **2019,** *7* (9), 4977-4987.

18. Ran, C.; Xu, J.; Gao, W.; Huang, C.; Dou, S., Defects in Metal Triiodide Perovskite Materials Towards High-Performance Solar Cells: Origin, Impact, Characterization, and Engineering. *Chem. Soc. Rev.* **2018,** *47* (12), 4581-4610.

19. Tavakoli, M. M.; Dastjerdi, H. T.; Prochowicz, D.; Yadav, P.; Tavakoli, R.; Saliba, M.; Fan, Z.; Highly efficient and stable inverted perovskite solar cells using down-shifting quantum dots as a light management layer and moisture-assisted film growth. *J. Mater. Chem. A*, **2019**, *7* (24), 14753-14760.

20. Berhe, T. A.; Su, W.-N.; Chen, C.-H.; Pan, C.-J.; Cheng, J.-H.; Chen, H.-M.; Tsai, M.-C.; Chen, L.-Y.; Dubale, A. A.; Hwang, B.-J., Organometal Halide Perovskite Solar Cells: Degradation and Stability. *Energy Environ. Sci.* **2016,** *9* (2), 323-356.

21. Zheng, X.; Chen, B.; Dai, J.; Fang, Y.; Bai, Y.; Lin, Y.; Wei, H.; Zeng, Xiao C.; Huang, J., Defect Passivation in Hybrid Perovskite Solar Cells using Quaternary Ammonium Halide Anions and Cations. *Nat. Energy* **2017,** *2* (7), No. 17102.

22. Jeon, N. J.; Noh, J. H.; Yang, W. S.; Kim, Y. C.; Ryu, S.; Seo, J.; Seok, S. I., Compositional Engineering of Perovskite Materials for High-Performance Solar Cells. *Nature* **2015,** *517*, 476-480.

23. Bu, T. L.; Liu, X. P.; Zhou, Y.; Yi, J. P.; Huang, X.; Luo, L.; Xiao, J. Y.; Ku, Z. L.; Peng, Y.; Huang, F. Z.; Cheng, Y. B.; Zhong, J., A Novel Quadruple-Cation Absorber for Universal Hysteresis Elimination for High Efficiency and Stable Perovskite Solar Cells. *Energy Environ. Sci.* **2017,** *10* (12), 2509-2515.

24. Zhao, J.; Tavakolib, R.; Tavakoli, M. M.; Synergistic interface and compositional engineering of inverted perovskite solar cells enables highly efficient and stable photovoltaic devices. *Chem. Commun*., **2019**,*55* (62), 9196-9199.

25. Yue, S.; Lu, S.; Ren, K.; Liu, K.; Azam, M.; Cao, D.; Wang, Z.; Lei, Y.; Qu, S.; Wang, Z., Insights into the Influence of Work Functions of Cathodes on Efficiencies of Perovskite Solar Cells. *Small* **2017,** *13*(19), 1700007.

26. Zhou, H.; Chen, Q.; Li, G.; Luo, S.; Song, T.-b.; Duan, H.-S.; Hong, Z.; You, J.; Liu, Y.; Yang, Y., Interface Engineering of Highly Efficient Perovskite Solar Cells. *Science* **2014,** *345* (6196), 542-546.

27. Tavakoli, M. M.; Bi, D.; Pan, L.; Hagfeldt, A.; Zakeeruddin, S. M.; Grätzel, M., Adamantanes Enhance the Photovoltaic Performance and Operational Stability of Perovskite Solar Cells by Effective Mitigation of Interfacial Defect States. *Adv. Energy Mater.* **2018**, *8* (19), 1800275.

28. Jeon, N. J.; Noh, J. H.; Kim, Y. C.; Yang, W. S.; Ryu, S.; Seok, S. I., Solvent Engineering For High-Performance Inorganic-Organic Hybrid Perovskite Solar Cells. *Nat. Mater.* **2014,** *13* (9), 897-903.

29. Wu, T.; Wang, Y.; Li, X.; Wu, Y.; Meng, X.; Cui, D.; Yang, X.; Han, L., Efficient Defect Passivation for Perovskite Solar Cells by Controlling the Electron Density Distribution of Donor-π-Acceptor Molecules. *Adv. Energy Mater.* **2019**, *9* (17), 1803766.

30. Zhang, H.; Wu, Y.; Shen, C.; Li, E.; Yan, C.; Zhang, W.; Tian, H.; Han, L.; Zhu, W.-H., Efficient and Stable Chemical Passivation on Perovskite Surface via Bidentate Anchoring. *Adv. Energy Mater.* **2019**, *9* (13),1803573.

31. Zhao, Y.; Wei, J.; Li, H.; Yan, Y.; Zhou, W.; Yu, D.; Zhao, Q., A Polymer Scaffold for Self-Healing Perovskite Solar Cells. *Nat. Commun.* **2016,** *7*, No. 10228.

32. Xu, J.; Buin, A.; Ip, A. H.; Li, W.; Voznyy, O.; Comin, R.; Yuan, M.; Jeon, S.; Ning, Z.; McDowell, J. J.; Kanjanaboos, P.; Sun, J. P.; Lan, X.; Quan, L. N.; Kim, D. H.; Hill, I. G.; Maksymovych, P.; Sargent, E. H., Perovskite-Fullerene Hybrid Materials Suppress Hysteresis In Planar Diodes. *Nat. Commun.* **2015,** *6*, No. 7081.

33. Azam, M.; Liu, K.; Yue, S.; Sun, Y.; Zhang, D.; Hassan, A.; Wang, Z.; Zhou, H.; Qu, S.; Wang, Z., The Positive Function of Incorporation of Small Molecules into Perovskite Materials for High-Efficient Stable Solar Cells. *Sol. RRL* **2019,** *3* (3), 1800327.

34. Guo, Y.; Sato, W.; Shoyama, K.; Nakamura, E., Sulfamic Acid-Catalyzed Lead Perovskite Formation for Solar Cell Fabrication on Glass or Plastic Substrates. *J. Am. Chem. Soc.* **2016,** *138* (16), 5410-5416.

35. Zhang, W.; Saliba, M.; Stranks, S. D.; Sun, Y.; Shi, X.; Wiesner, U.; Snaith, H. J., Enhancement of Perovskite-Based Solar Cells Employing Core–Shell Metal Nanoparticles. *Nano Lett.* **2013,** *13* (9), 4505-4510.

36. Zhang, J.; Wu, S.; Liu, T.; Zhu, Z.; Jen, A. K. Y., Boosting Photovoltaic Performance for Lead Halide Perovskites Solar Cells with BF^{4-} Anion Substitutions. *Adv. Funct. Mater.* **2019**, *29* (47),1808833.

37. Tang, A.; Xiao, B.; Chen, F.; Zhang, J; Wei, Z.; Zhou, E., The Introduction of Fluorine and Sulfur Atoms into Benzotriazole-Based p-Type Polymers to Match with a Benzotriazole-Containing n-Type Small Molecule: "The Same-Acceptor-Strategy" to Realize High Open-Circuit Voltage. *Adv. Energy Mater*. **2018**, *8* (25), 1801582.

38. Tang, A.; Song, W.; Xiao, B.; Guo, J.; Min, J.; Ge, Z.; Zhang, J.; Wei, Z.; Zhou, E. Benzotriazole-Based Acceptor and Donors, Coupled with Chlorination, Achieve a High V_{OC} of 1.24 V and an Efficiency of 10.5% in Fullerene-Free Organic Solar Cells. *Chem. Mater.* **2019**, *31* (11), 3941–3947.

39. Tang, A.; Xiao, B.; Wang, Y.; Gao, F.; Tajima, K.; Bin, H.; Zhang, Z.-G.; Li, Y.; Wei, Z.; Zhou, E., Simultaneously Achieved High Open-Circuit Voltage and Efficient Charge Generation by Fine-Tuning Charge-Transfer Driving Force in Nonfullerene Polymer Solar Cells. *Adv. Funct. Mater.* **2017**, *28* (6), 1704507.

40. Zhao, W.; Li, S.; Yao, H.; Zhang, S.; Zhang, Y.; Yang, B.; Hou, J.; Molecular Optimization Enables over 13% Efficiency in Organic Solar Cells. *J. Am. Chem. Soc*. **2017**, *139* (21), 7148−7151.

41. Yu, J.; Wang, N.; Zang, Y.; Jiang, Y., Organic Photovoltaic Cells Based on Tpbi as a Cathode Buffer Layer. *Sol. Energy Mater. Sol. Cells* **2011,** *95* (2), 664-668.

42. Yue, S. Z.; Liu, K.; Xu, R.; Li, M. C.; Azam, M.; Ren, K.; Liu, J.; Sun, Y.; Wang, Z. J.; Cao, D. W.; Yan, X. H.; Qu, S. C.; Lei, Y.; Wang, Z. G., Efficacious Engineering on Charge Extraction for Realizing Highly Efficient Perovskite Solar Cells. *Energy Environ. Sci.* **2017,** *10* (12), 2570-2578.

43. Li, Y.; Meng, L.; Yang, Y. M.; Xu, G.; Hong, Z.; Chen, Q.; You, J.; Li, G.; Yang, Y.; Li, Y., High-Efficiency Robust Perovskite Solar Cells on Ultrathin Flexible Substrates. *Nat. Commun.* **2016,** *7*, No. 10214.

44. Zhao, J.; Deng, Y.; Wei, H.; Zheng, X.; Yu, Z.; Shao, Y.; Shield, J. E.; Huang, J., Strained Hybrid Perovskite Thin Films and their Impact on the Intrinsic Stability of Perovskite Solar Cells. *Sci. Adv.* **2017,** *3* (11), eaao5616.

45. Song, C.; Li, X.; Wang, Y.; Fu, S.; Wan, L.; Liu, S.; Zhang, W.; Song, W.; Fang, J. Sulfonyl-based Nonfullerene Electron-Acceptor Assisted Grain Boundary Passivation for Efficient and Stable Perovskite Solar Cells. *J. Mater. Chem. A* **2019**, *7* (34), 19881-19888.

46. Liu, C.; Huang, Z.; Hu, X.; Meng, X.; Huang, L.; Xiong, J.; Tan, L.; Chen, Y. Grain Boundary Modification via F4TCNQ To Reduce Defects of Perovskite Solar Cells with Excellent Device Performance. *ACS Appl. Mater. Interfaces* **2018**, *10* (2), 1909−1916.

47. Niu, T.; Lu, J.; Munir, R.; Li, J.; Barrit, D.; Zhang, X.; Hu, H.; Yang, Z.; Amassian, A.; Zhao, K.; Liu, S. F. Stable High‐Performance Perovskite Solar Cells via Grain Boundary Passivation. *Adv. Mater*. **2018**, *30* (16), 1706576.

48. Groenewolt, M.; Antonietti, M. Synthesis of g-C_3N_4 Nanoparticles in Mesoporous Silica Host Matrices. *Adv. Mater*., **2005**, 17 (14), 1789–1792.

49. Ng, T.-W.; Chan, C.-Y.; Lo, M.-F.; Guan, Z. Q.; Lee, C.-S., Formation Chemistry of Perovskites with Mixed Iodide/Chloride Content and the Implications on Charge Transport Properties. *J. Mater. Chem. A* **2015,** *3* (17), 9081-9085.

50. Yun, J. H.; Lee, I.; Kim, T.-S.; Ko, M. J.; Kim, J. Y.; Son, H. J., Synergistic Enhancement and Mechanism Study of Mechanical and Moisture Stability of Perovskite Solar Cells Introducing Polyethylene-Imine into the $CH_3NH_3PbI_3$/HTM Interface. *J. Mater. Chem. A* **2015,** *3* (44), 22176-22182.

51. Li, Z.; Xiao, C.; Yang, Y.; Harvey, S. P.; Kim, D. H.; Christians, J. A.; Yang, M.; Schulz, P.; Nanayakkara, S. U.; Jiang, C.-S.; Luther, J. M.; Berry, J. J.; Beard, M. C.; Al-Jassim, M. M.; Zhu, K., Extrinsic Ion Migration in Perovskite Solar Cells. *Energy Environ. Sci.* **2017,** *10* (5), 1234-1242.

52. Lee, J. W.; Kim, S. G.; Bae, S. H.; Lee, D. K.; Lin, O.; Yang, Y.; Park, N. G., The Interplay between Trap Density and Hysteresis in Planar Heterojunction Perovskite Solar Cells. *Nano Lett.* **2017,** *17* (7), 4270-4276.

53. Rose, A., Space-Charge-Limited Currents in Solids. *Phy. Rev.* **1955,** *97* (6), 1538-1544.

54. Wehrenfennig, C.; Liu, M.; Snaith, H. J.; Johnston, M. B.; Herz, L. M., Charge-Carrier Dynamics in Vapour-Deposited Films of the Organolead Halide Perovskite $CH_3NH_3PbI_{3-X}cl_x$. *Energy Environ. Sci.* **2014,** *7* (7), 2269-2275.

55. Tan, F.; Tan, H.; Saidaminov, M. I.; Wei, M.; Liu, M.; Mei, A.; Li, P.; Zhang, B.; Tan, C. S.; Gong, X.; Zhao, Y.; Kirmani, A. R.; Huang, Z.; Fan, J. Z.; Quintero-Bermudez, R.; Kim, J.; Zhao, Y.; Voznyy, O.; Gao, Y.; Zhang, F.; Richter, L. J.; Lu, Z. H.; Zhang, W.; Sargent, E. H., In Situ Back-Contact Passivation Improves Photovoltage and Fill Factor in Perovskite Solar Cells. *Adv. Mater.* **2019,** *31* (14), e1807435.

56. Chiang, C.-H.; Wu, C.-G., Bulk Heterojunction Perovskite–PCBM Solar Cells With High Fill Factor. *Nat. Photonics* **2016,** *10* (3), 196-200.

57. Huang, J.; Tan, S.; Lund, P. D.; Zhou, H., Impact of H_2O on Organic–Inorganic Hybrid Perovskite Solar Cells. *Energy Environ. Sci.* **2017,** *10* (11), 2284-2311.

58. Zhu, Z.; Hadjiev, V. G.; Rong, Y.; Guo, R.; Cao, B.; Tang, Z.; Qin, F.; Li, Y.; Wang, Y.; Hao, F.; Venkatesan, S.; Li, W.; Baldelli, S.; Guloy, A. M.; Fang, H.; Hu, Y.; Yao, Y.; Wang, Z.; Bao, J., Interaction of Organic Cation with Water Molecule in Perovskite MAPbI3: From Dynamic Orientational Disorder to Hydrogen Bonding. *Chem. Mater.* **2016,** *28* (20), 7385-7393.

59. Liu, Y.; Palotas, K.; Yuan, X.; Hou, T.; Lin, H.; Li, Y.; Lee, S. T., Atomistic Origins of Surface Defects in $CH_3NH_3PbBr_3$ Perovskite and their Electronic Structures. *ACS Nano* **2017,** *11* (2), 2060-2065.

Table of Contents Graphic (TOC)